Computers in Biology and Medicine 41 (2011) 292–301

Contents lists available at ScienceDirect

Computers in Biology and Medicine

journal homepage: www.elsevier.com/locate/cbm

# Homogeneity- and density distance-driven active contours for medical image segmentation

Phan Tran Ho Truc [a], Tae-Seong Kim [b], Sungyoung Lee [a], Young-Koo Lee [a,*]

[a] Department of Computer Engineering, Kyung Hee University, Repuplic of Korea
[b] Department of Biomedical Engineering, Kyung Hee University, Republic of Korea

ARTICLE INFO

*Article history:*
Received 26 January 2010
Accepted 18 March 2011

*Keywords:*
Active contours
Image segmentation
Level set methods
Medical images

ABSTRACT

In this paper, we present a novel active contour (AC) model for medical image segmentation that is based on a convex combination of two energy functionals to both minimize the inhomogeneity within an object and maximize the distance between the object and the background. This combination is necessary because objects in medical images, e.g., bones, are usually highly inhomogeneous while distinct organs should generate distinct image configurations. Compared with the conventional Chan–Vese AC, the proposed model yields similar performance in a set of CT images but performs better in an MRI data set, which is generally in lower contrast.



## 1. Introduction

Medical image analysis has played a more and more important role in many clinical procedures due to the advancements in medical imaging modalities such as computed tomography (CT), magnetic resonance imaging (MRI), and ultrasound [1]. Medical image analysis deals with enhancement, segmentation, registration, and visualization, among which segmentation is a very crucial task because it provides the organ of interest, such as bone [2,3], brain [4], or heart [5], that is necessary for clinical diagnosis and/or treatment [6]. Image segmentation is to partition the image into its constituent parts which correspond to separated objects. One then may think of the extraction of object boundaries, where simple edge detectors like the gradient-based and the second-order derivative-based operators [7] or a more elaborated approach like Canny edge detector [8] are widely used. However, an edge detector is usually not suitable for extracting object boundaries due to many reasons. Firstly, extracted edges do not always correspond to object boundaries. For example, one may think of texture. Secondly, edge detectors usually yield discontinued edges, whereas objects are necessarily separated by closed contours. So post-processing tasks are needed to link discontinued edges, which are complex and prone to be erroneous. Finally, edge detectors depend on the local information in a neighborhood of a pixel. Being local is sometimes advantageous, yet in many cases, the global view of the object appearance is of significant clues. Therefore, image segmentation in general is different from edge detection. The former is to provide regions, represented by closed boundaries, not edges.

*Region growing* [7,9] is one of the simple techniques that provide regions. Starting with a set of seed points, the algorithm successively appends to each seed point its neighboring pixels that share similar image features such as intensity, texture, or color to form larger regions. This is an iterative process that stops when all pixels are processed. The algorithm can be regarded as a heuristic minimization for the Mumford-Shah functional [10] where the energy decreases while the regions are growing. Therefore, just like its energy optimization counterpart, region growing suffers from the sensitivity to seed selection as the initial condition, which can lead to under- or over-growing.

Another region-providing method is *snake* or *active contour* (AC). An AC model is the description of contours in 2D or surfaces in 3D which evolve under an appropriate energy to move toward desired features, such as object boundaries. Because contours are always closed, object boundaries extracted are continuous, making post-processing tasks to connect discontinued edges no longer necessary. Since it was first introduced by Kass, Witkin, and Terzopoulos [11], active contour has attracted a large amount of researches: many AC models have been proposed, which can be categorized into parametric-type and geometric-type ACs. In parametric ACs [11–15], the curve (contour) $C$ is explicitly represented using its parameterization: $C(p) = [x(p), y(p)]$, where $p(0 \le p \le 1)$ parameterizes the curve. This makes the parametric ACs non-intrinsic because their energy functional depends on the parameterizations but not on the geometry of the contour. As a result, these models cannot naturally handle topological changes to simultaneously detect multiple objects. Many special (usually heuristic) procedures have been proposed in detecting possible splitting and merging [16–18] but prior knowledge about the number of objects needs to be given.

* Corresponding author. Fax: +82 31 202 2520.
*E-mail address:* yklee@khu.ac.kr (Y.-K. Lee).
*URL:* http://uclab.khu.ac.kr (Y.-K. Lee).

0010-4825/$ - see front matter © 2011 Elsevier Ltd. All rights reserved.
doi:10.1016/j.compbiomed.2011.03.006

Geometric-type ACs [19–24], on the other hand, can handle topological changes without additional efforts because they are implemented using level-set framework [25,26]. In this framework, the curve $C$ is implicitly represented by the zero level set of a function $\phi(\mathbf{x},t):\mathbb{R}^n\times[0,\infty)\to\mathbb{R}$, $n=\{2,3\}$ such that

$$C=\{\mathbf{x}\in\mathbb{R}^n:\phi(\mathbf{x},t)=0\}. \quad (1)$$

The function $\phi$ is then evolved using the following general equation

$$\frac{\partial\phi}{\partial t}=\underbrace{b\kappa|\nabla\phi|}_{\text{Curvature Based}}+\underbrace{V_N|\nabla\phi|}_{\text{Normal Direction}}+\underbrace{\vec{S}\cdot\nabla\phi}_{\text{Vector Field Based}}, \quad (2)$$

where $\kappa$ is the Euclidean curvature and ($b$, $V_N$, and $\vec{S}$) are three parameters determining the velocity and direction of the evolution. The curvature-based force is to smooth the curve; the normal direction force shrinks or expands the curve along its normal direction; and the external vector field-based force acts as a translation operator. Although the function $\phi$ itself moves up and down on a fixed coordinate system without changing its topology, its zero level set (or the curve $C$) may automatically split or merge.

The first geometric-type AC is the (original) *Geometric AC* which was introduced independently by Caselles et al. [19] and Malladi et al. [27]. The main idea is to move the curve using the curvature and the normal direction forces and stop the motion at the object boundaries using an edge-based function $g(\mathbf{x})=g(|\nabla I|^2)$ (where $\nabla I$ is the gradient of the input image $I$) which approaches 0 on the edges and 1 otherwise, e.g., $g(\mathbf{x})=e^{-(1/\sigma_e^2)|\nabla G_\sigma * I(\mathbf{x})|^2}$ with $\sigma_e$ a scaling factor and $G_\sigma$ the smoothing Gaussian kernel of scale $\sigma$. Caselles et al. [20] proposed another geometric-type AC, called *Geodesic AC*, using an energy functional to search for a curve of minimal edge-weighted length (geodesic curve). This model is similar to the Geometric AC, except that $\nabla g$ is used as a vector field force to increase the curve attraction towards weak edges. Then, Paragios et al. [24] proposed to replace the vector field force $\nabla g$ with the well-known gradient vector flow (GVF) introduced by Xu and Prince [15] to increase the capture range, leading to the *GVF Fast Geometric AC* (shortly, GVF-Geo AC). Differently, Chan and Vese [22] proposed a new model, which we call the *CV AC*, using an approximation of the Mumford-Shah functional. All these geometric-type ACs are considered as classical models in the research field and their level-set parameters are summarized in Table 1. Here, we do not consider other approaches that incorporate prior knowledge about object shape [28–30] or texture [31] since they require a training stage which is generally application specific.

We can see from Table 1 that the first three models depend heavily on the edge function $g(\mathbf{x})$, making themselves prone to be trapped in false edges caused by noises. This can be alleviated by performing smoothing with larger $\sigma$, yet it in turn leads to inexact results because edges are smoothed as well. The CV AC, on the other hand, does not depend on $g$ (this gives it the name "without-edge AC") but on the homogeneity assumption, i.e., image features within a segment should be similar. In this case, the image $I$ is assumed to be consisted of two segments with approximately piecewise-constant intensities. The CV energy functional $F(C)$ is defined as

$$F(C)=F_1(C)+F_2(C)=\int_{inside(C)}|I(\mathbf{x})-c_{in}|^2\mathrm{d}\mathbf{x}+\int_{outside(C)}|I(\mathbf{x})-c_{out}|^2\mathrm{d}\mathbf{x}, \quad (3)$$

where $c_{in}$ and $c_{out}$ are, respectively, the average intensities inside and outside the variable curve $C$. Compared to the other three AC models, the CV AC can detect the objects more exactly since it does not need to smooth the initial image (via the edge function $g(|\nabla I_\sigma|^2)$ where $I_\sigma=G_\sigma * I$), even if it is very noisy. In other words, this model is more robust to noise and thus suitable for medical images since they are often noisy and low contrast. Also, it was shown to provide a relaxed initial position requirement [22].

However, the convergence of the CV AC depends on the homogeneity of the segmented objects. When the inhomogeneity becomes large like in carpal bones or knee bones, the CV AC provides unsatisfactory results. To address this, let us consider a synthetic image (size $128\times128$) with an inhomogeneous object having five different parts over the bright background as shown in Fig. 1. The image intensity is scaled on the range [0, 1], with 1 the brightest. The CV fitting term $F(C)$ is calculated at each iteration during the evolution and plotted in Fig. 2.[1] As expected, the curve moves in the direction of decreasing $F(C)$ and stops when $F(C)$ reaches a minimum value, which is $F(C^*)=34$ (at iteration number 16) in this case. Nevertheless, this is not the "desirable" result, whose minimum fitting term is $F(C^{des})=197$. Clearly, the desirable minimum here is larger (more local) than the practically resulting minimum $F(C^*)$.

From the above example, we can see that the global minimum of the CV energy functional does not always guarantee the desirable results, especially when a segment is highly inhomogeneous. To provide flexibility in searching for the desirable minimum (which is often neither the most local nor global), Li and Yezzi [32] proposed a *dual-front AC* model with the active region's width as a controlling factor. The model is an iterative process consisting of the active region relocation and the dual front evolution which is another iterative process, demanding a high computational cost.

Vese and Chan [23] and Tsai et al. [33] independently and contemporaneously proposed to use the original Mumford-Shah functional [10] to segment inhomogeneous objects. Because the minimizer of the Mumford-Shah functional is difficult to get (and remains an issue) due to the term of discontinuities, the authors in [23,33] presented the set of discontinuities in form of a curve evolution problem. The resulting optimization process involves both evolving a level-set function and solving Poison partial differential equations. Although it can generate a piecewise smooth approximation of the input image that well represents the objects of interest, this process is very complicated and computationally expensive and requires a good initialization. Another piecewise smooth approach was presented in [34]. The authors elegantly generalized the mean intensities $c_{in}$ and $c_{out}$ in (3) to the local weighted averaging using a Gaussian kernel convolution. This leads to a model that approximates the original Mumford-Shah functional but has a complexity close to that of the CV model. When the variance of the Gaussian kernel approaches infinity, this model becomes the CV model. On one hand, this variance parameter

**Table 1**
Level-set parameters of the classical AC models.

| | $b$ | $V_N$ | $\vec{S}$ |
|---|---|---|---|
| Geometric | $g(\mathbf{x})$ | $\eta g(\mathbf{x})$ | $\vec{0}$ |
| Geodesic | $g(\mathbf{x})$ | $\eta g(\mathbf{x})$ | $\nabla g(\mathbf{x})$ |
| GVF-Geo | $g(\mathbf{x})$ | $\eta K(\mathbf{x})g(\mathbf{x})$ | $g(\mathbf{x})(1-\lvert K(\mathbf{x})\rvert)[\hat{u},\hat{v}]$ |
| CV | $\gamma$ | $\eta+(I-c_{in})^2-(I-c_{out})^2$ | $\vec{0}$ |

$\gamma$ and $\eta$ are constants, $[\hat{u},\hat{v}]$ the GVF [15], $K(\mathbf{x})$ a function depending on the curve normal and the GVF, $I=I(\mathbf{x})$ the image intensity, and $c_{in}$ and $c_{out}$, respectively, the average intensity values inside and outside the variable curve.

[1] Note that Fig. 2 plots only the term $F(C)$ in (3), whereas the result in Fig. 1 was obtained from the original CV model [22] that includes both $F(C)$ and a length term to guarantee the smoothness of the contour.

**Fig. 1.** CV AC failure on capturing an inhomogeneous object, cpu = 58 s. Left to right: initial ($F(C) = 645$), intermediate (312), final (34), and desired position (197). The plot of $F(C)$ at every iteration is given in Fig. 2.

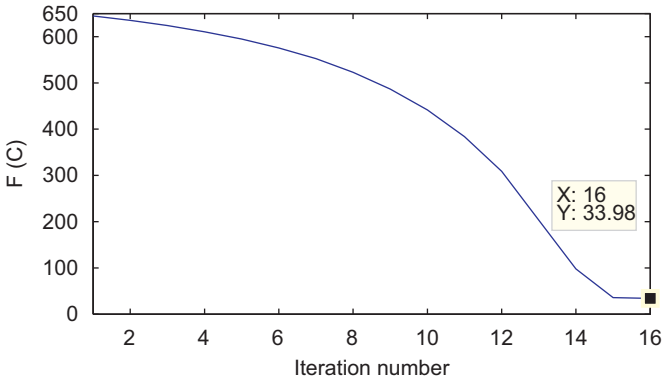


**Fig. 2.** CV fitting term $F(C)$ at every iteration of the CV AC evolution process. The obtained minimum ($\approx 34$) is not the "desirable" one ($\approx 197$).

provides a great flexibility to segment objects with large range of inhomogeneity levels, but on the other hand, it requires much user interaction to decide the right value to work with the problem at hand. Estimation of a varying optimal variance remains unsolved.

Alternatively, this paper presents a novel AC model[2] to tackle the problem of CV AC. The reason CV AC fails is that in this model, a segment is represented by only its mean value, which is not sufficient for a highly inhomogeneous object. If one considers segmentation as a classification problem, i.e., a specific pixel needs to be classified into either the object or the background, the CV model resembles a classification solution where the difference within each class is minimized. The proposed model, on the other hand, uses the whole density function instead of only the mean value (as in (3)). Here, we assume that the density function of one object should be different from that of another. This is true, especially for medical imagery, because distinct organs shall generate distinct configurations in a medical image. The difference between density functions is reflected as an additional energy term into the CV fitting term $F(C)$ in order to balance the differences within every segment and the distances between separate segments. By properly weighting the two terms, the new evolution flow, which is implemented in a level-set framework, can flexibly drive the contour towards the desirable position without the overhead required by the iterative dual-front evolution [32]. From a classification's perspective, the proposed flow searches for a classifier that provides optimal classification errors since it both minimizes the error within one class and maximizes the distances between classes.

The rest of the paper is organized as follows. We formulate our model as an energy optimization and derive its level-set formulation and implementation in the next section. Then, in Section 3, we describe the testing data sets and the quantitative measures we use to evaluate the proposed model. Section 4 presents evaluation results of our model in comparison with the conventional CV AC. Finally, we summarize and conclude the paper in Section 5.

[2] The conference version of the proposed work was presented at EMBC 2008 [35].

## 2. The proposed AC model

### 2.1. Mathematical derivation

Our approach is to incorporate an additional density distance term into the CV fitting term $F(C)$. Although there are alternative measures defining the distance between probability distributions such as the Fisher ratio, the Kullback–Leibler divergence [36], and the Wasserstein distance [37], we choose the Bhattacharyya distance for both its better performance in applications of signal selection as observed in [38] and its simple analytical form. Another advantage of this measure over the Fisher ratio and the Wasserstein distance is that it works with arbitrary distributions, whereas the Fisher ratio requires mean-separated distributions to yield good results [39, p. 132] and the Wasserstein distance-based segmentation model [37] assumes an independently identical distributed image intensity. Also, the Bhattacharyya distance has recently been successfully applied in computer vision [40], object tracking [41,42], and image segmentation [43]. In [40], it was shown as an efficient contrast parameter between the target and background whose distributions' parameters are unknown. Based on this observation, the authors in [41,43] formulated the distance in form of an active contour term to extract the natural shape of the object as opposed to the pre-defined elliptical shape assumed in [42]. Specifically, in the active contour framework, the Bhattacharyya distance between the density functions inside and outside the curve $C$, i.e., $p_{in}(z)$ and $p_{out}(z)$, $z \in \mathbb{R}^n$, is defined as $[-\log\ B(C)]$ where $B(C) \equiv B = \int_{\mathbb{R}^n} \sqrt{p_{in}(z)p_{out}(z)}dz$ and thus the maximization of this distance is equivalent to the minimization of $B(C)$. The additional term $B(C)$ is incorporated as

$$E_0(C) = \beta F(C) + (1-\beta)B(C), \tag{4}$$

where $\beta \in [0,1]$. Note that to be comparable to the $F(C)$ term, in our implementation, $B(C)$ is multiplied by the area of the image because its value is always within the interval [0, 1], whereas $F(C)$ is calculated based on the integral over the image plane. As usual [22], we regularize the solution by constraining the length of the curve and the area of the region inside it, yielding the total energy functional as

$$E(C) = \gamma Length(C) + \eta Area(inside(C)) + \beta F(C) + (1-\beta)B(C), \tag{5}$$

where $\gamma$ and $\eta$ are non-negative constants.

The intuition behind the proposed model, $\inf_C E(C)$, is that we seek for a curve which is regular (the first two terms) and partitions the image into two regions such that the differences within each region are minimized (the $F(C)$ term) and the distance between the two regions' density functions is maximized (the $B(C)$ term).

For the level-set formulation, let us define $\phi$ as the level-set function, $I:\Omega\to\mathcal{Z}\subset\mathbb{R}^n$ as a certain image feature such as intensity, color, texture, or a combination thereof, and $H(\cdot)$ and $\delta_0(\cdot)$ as the Heaviside and the Dirac functions, respectively.

$$H(u)=\begin{cases}1 & \text{if } u\geq 0\\ 0 & \text{if } u<0\end{cases}\quad \delta_0(u)=\frac{\mathrm{d}}{\mathrm{d}u}H(u). \tag{6}$$

The energy functional can then be rewritten as

$$\begin{aligned}E(\phi)=&\gamma\int_\Omega|\nabla H(\phi(\mathbf{x}))|\,\mathrm{d}\mathbf{x}+\eta\int_\Omega H(-\phi(\mathbf{x}))\,\mathrm{d}\mathbf{x}\\&+\beta\left[\int_\Omega|I(\mathbf{x})-c_{in}|^2H(-\phi(\mathbf{x}))\,\mathrm{d}\mathbf{x}+\int_\Omega|I(\mathbf{x})-c_{out}|^2H(\phi(\mathbf{x}))\,\mathrm{d}\mathbf{x}\right]\\&+(1-\beta)\int_{\mathcal{Z}}\sqrt{p_{in}(z)p_{out}(z)}\,\mathrm{d}z,\end{aligned} \tag{7}$$

where

$$\begin{aligned}p_{in}(z)&=\frac{\int_\Omega\delta_0(z-I(\mathbf{x}))H(-\phi(\mathbf{x}))\mathrm{d}\mathbf{x}}{\int_\Omega H(-\phi(\mathbf{x}))\mathrm{d}\mathbf{x}},\\ p_{out}(z)&=\frac{\int_\Omega\delta_0(z-I(\mathbf{x}))H(\phi(\mathbf{x}))\mathrm{d}\mathbf{x}}{\int_\Omega H(\phi(\mathbf{x}))\mathrm{d}\mathbf{x}}.\end{aligned} \tag{8}$$

In a general form, it reads

$$E(\phi)=\underbrace{\int_\Omega f(\phi,\phi_{x_1},\phi_{x_2},\ldots,\phi_{x_n})\,\mathrm{d}\mathbf{x}}_{\tilde{F}(\phi)}+(1-\beta)B(\phi), \tag{9}$$

where $\mathbf{x}=[x_1,x_2,\ldots,x_n]\in\mathbb{R}^n$, $\phi_{x_i}=\partial\phi/\partial x_i$, $i=\overline{1..n}$, $B(\phi)=\int_{\mathcal{Z}}\sqrt{p_{in}(z)p_{out}(z)}\,\mathrm{d}z$, and $f=\gamma\delta_0(\phi)|\nabla\phi|+\eta H(-\phi)+\beta|I-c_{in}|^2\,H(-\phi)+\beta|I-c_{out}|^2H(\phi)$.

The first variation (w.r.t $\phi(\mathbf{x})$) is given by

$$\frac{\delta E}{\delta\phi}=\frac{\delta\tilde{F}}{\delta\phi}+(1-\beta)\frac{\delta B}{\delta\phi}. \tag{10}$$

Using Euler–Lagrange equation, one has

$$\frac{\delta\tilde{F}}{\delta\phi}=\frac{\partial f}{\partial\phi}-\sum_{i=1}^{n}\frac{\partial}{\partial x_i}\frac{\partial f}{\partial\phi_{x_i}}=\delta_0(\phi)[-\eta-\beta(I-c_{in})^2+\beta(I-c_{out})^2-\gamma\kappa]. \tag{11}$$

On the other hand,

$$\frac{\delta B}{\delta\phi}=\frac{1}{2}\int_{\mathcal{Z}}\left(\frac{\partial p_{in}(z)}{\partial\phi}\sqrt{\frac{p_{out}(z)}{p_{in}(z)}}+\frac{\partial p_{out}(z)}{\partial\phi}\sqrt{\frac{p_{in}(z)}{p_{out}(z)}}\right)\mathrm{d}z, \tag{12}$$

where $p_{in}(z)$ and $p_{out}(z)$ are given in (8). Differentiating them w.r.t $\phi(\mathbf{x})$, one obtains

$$\begin{aligned}\frac{\partial p_{in}(z)}{\partial\phi}&=\frac{\delta_0(\phi)}{A_{in}}[p_{in}(z)-\delta_0(z-I)],\\ \frac{\partial p_{out}(z)}{\partial\phi}&=\frac{\delta_0(\phi)}{A_{out}}[\delta_0(z-I)-p_{out}(z)],\end{aligned} \tag{13}$$

where $A_{in}$ and $A_{out}$ are, respectively, the areas inside and outside the contour and are given by

$$A_{in}=\int_\Omega H(-\phi(\mathbf{x}))\,\mathrm{d}\mathbf{x},\quad A_{out}=\int_\Omega H(\phi(\mathbf{x}))\,\mathrm{d}\mathbf{x}. \tag{14}$$

Substituting (13) into (12) and taking some simple modifications, one obtains

$$\frac{\delta B}{\delta\phi}=\delta_0(\phi)V(\mathbf{x}), \tag{15}$$

where

$$V(\mathbf{x})=\frac{B}{2}\left(\frac{1}{A_{in}}-\frac{1}{A_{out}}\right)+\frac{1}{2}\int_{\mathcal{Z}}\delta_0(z-I(\mathbf{x}))\left(\frac{1}{A_{out}}\sqrt{\frac{p_{in}(z)}{p_{out}(z)}}-\frac{1}{A_{in}}\sqrt{\frac{p_{out}(z)}{p_{in}(z)}}\right)\mathrm{d}z. \tag{16}$$

Combining (10), (11), and (15), one can derive the first variation of $E(\phi)$ as

$$\frac{\partial E}{\partial\phi}=\delta_0(\phi)[-\gamma\kappa-\eta-\beta(I-c_{in})^2+\beta(I-c_{out})^2+(1-\beta)V]. \tag{17}$$

Hence, the evolution flow associated with minimizing the energy functional in (7) is given by

$$\begin{aligned}\frac{\partial\phi}{\partial t}&=-\frac{\delta E}{\delta\phi}\\&=\delta_0(\phi)\left\{\gamma\kappa+\eta+\beta[(I-c_{in})^2-(I-c_{out})^2]-(1-\beta)\left[\frac{B}{2}\left(\frac{1}{A_{in}}-\frac{1}{A_{out}}\right)\right.\right.\\&\quad\left.\left.+\frac{1}{2}\int_{\mathcal{Z}}\delta_0(z-I)\left(\frac{1}{A_{out}}\sqrt{\frac{p_{in}}{p_{out}}}-\frac{1}{A_{in}}\sqrt{\frac{p_{out}}{p_{in}}}\right)\mathrm{d}z\right]\right\}.\end{aligned} \tag{18}$$

### 2.2. Implementation

There are a couple of possible regularizations of function $H$ (and $\delta_0$) [22,44] which determine the number of level curves that the evolution flow for $\phi$ acts on. Some regularizations make the flow acts on a few level curves around the zero level set $\{\phi(\mathbf{x})=0\}$ whilst some others acts on all level curves. In this paper, we choose to replace $\delta_0(\phi)$ by $|\nabla\phi|$ to extend the evolution to all level sets of $\phi$ as suggested in [44].

The pseudo-code for the proposed algorithm can be outlined as follows:

- $k=0$, initialize $\phi^k$ by $\phi_0$.
- Compute the mean values $c_{in}$ and $c_{out}$.
- Compute $p_{in}(z)$ and $p_{out}(z)$ according to (8).
- Compute $A_{in}$ and $A_{out}$ by (14).
- Evolve the curve using (18) to obtain $\phi^{k+1}$.
- Reinitialize $\phi$ as the signed distance function of the current curve (see [26] for details).
- Check whether convergence is met. If not, $k=k+1$ and go back to the second step.

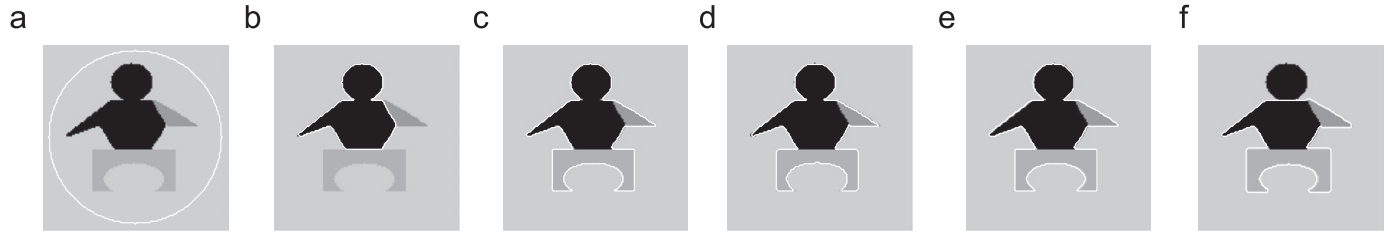


**Fig. 3.** Results of the proposed AC applied on the example image in Fig. 1 using $\gamma=0.3$ and various values of $\beta$: (a) initial curve in white, (b) final curve with $\beta=1.0$ (purely CV term), cpu = 57 s, (c) $\beta=0.8$, cpu = 21 s, (d) $\beta=0.5$, cpu = 71 s, (e) $\beta=0.3$, cpu = 18 s, and (f) $\beta=0.0$ (purely Bhattacharyya term), cpu = 25 s. The whole body is segmented correctly with a large range of $\beta$, i.e., (c)–(e).

Note that for digital images, $p_{in}(z)$ and $p_{out}(z)$ are nothing but the histograms. Note also that the integral in (18) can be easily calculated as follows.

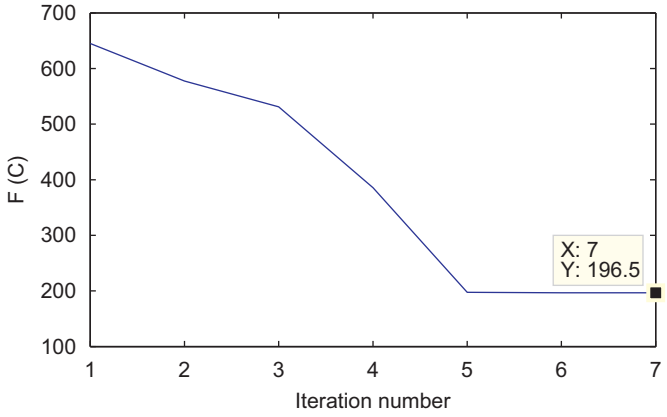


**Fig. 4.** CV fitting term $F(C)$ at every iteration of the proposed AC's evolution process with $\beta = 0.5$. The "desirable" minimum is found.

$\forall \mathbf{x}_0 \in \Omega$, find in the histograms $p_{in}(z)$ and $p_{out}(z)$ the $z_0$ such that $z_0 = I(\mathbf{x}_0)$. Then, the integral calculated at $x_0$ is $(1/A_{out})\sqrt{(p_{in}(z_0)/p_{out}(z_0))} - (1/A_{in})\sqrt{(p_{out}(z_0)/p_{in}(z_0))}$ if $p_{out}(z_0)p_{in}(z_0) \neq 0$. Otherwise, it is 0.

Therefore, although the proposed evolution flow looks complicated, its computation is straightforward and the complexity is comparable to that of the piecewise constant model, which is an advantage over the piecewise smooth approaches [23,33].

## 3. Experimental setup

### 3.1. Testing data

For performance evaluation, we use four testing data sets. The first one is an MRI data set [45], consisting of 14 gray scale cardiac images. Each image is of size $150 \times 150$ and the endocardial contours of the left ventricle were manually annotated, which will be used as "ground truths" (see, e.g., Fig. 13). The second data set is a set of 16 CT bone images covering the knee region of a patient. The images are also gray scale and of size $151 \times 151$. A medical expert was asked to manually extract bones from those images, the results of which are

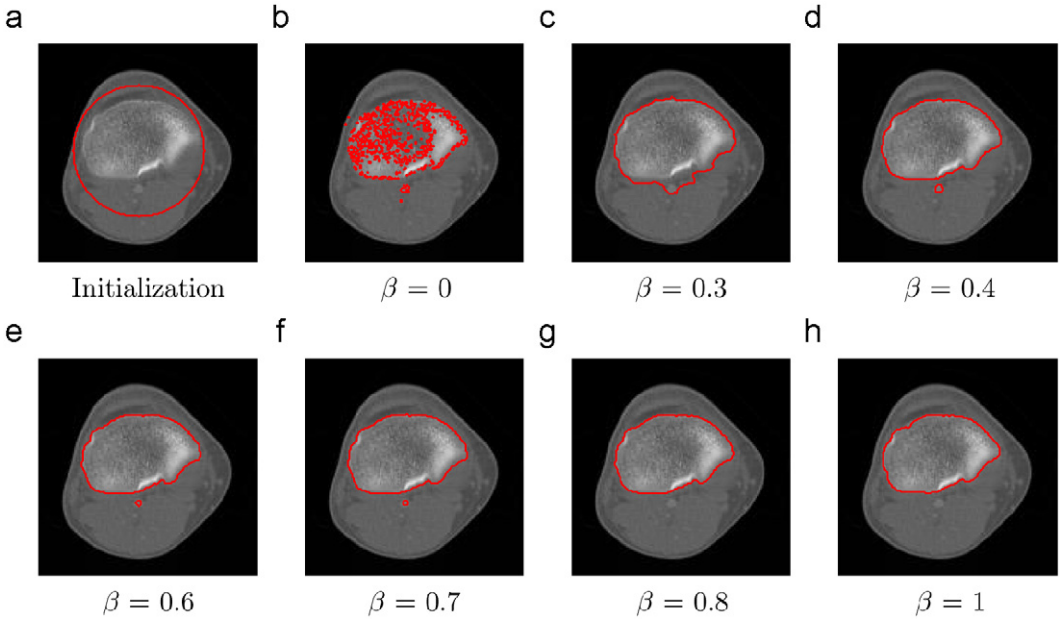


**Fig. 5.** Sample segmentation results of the proposed AC applied on an CT image using $\gamma = 0.1$ and various values of $\beta$. The bone structure is segmented correctly with many $\beta$ values, i.e., (d)–(f). This figure is in color in the electronic version.

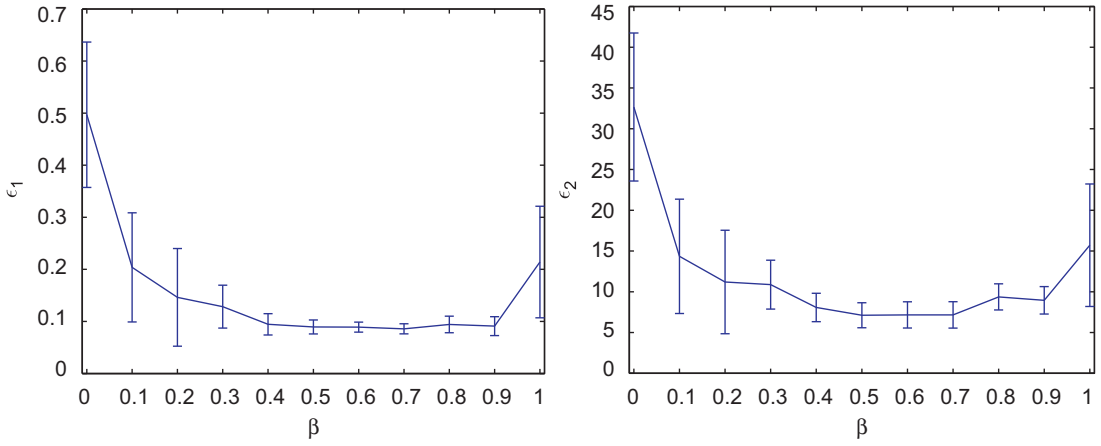


**Fig. 6.** Mean and SD plots of the error measures of the proposed AC applied on the real CT data set vs. $\beta$ values.

considered as "ground truths" (see, e.g., Fig. 12). Then, we created 16 corresponding synthetic images of size $100 \times 100$; each one adopts the extracted bone region as its foreground and has a homogeneous background whose intensity equals to the mean value of the extracted background in the corresponding CT image. These synthetic images were then used to generate the two other data sets, named Salt-pepper data set and Contrast data set (see, e.g., Figs. 7 and 10, respectively).

The Salt-pepper data set was created by adding salt and pepper noise of five different density values, $d = \{0, 0.05, 0.1, 0.2, 0.3\}$, to the 16 original synthetic images. So, this data set has 80 images (16 images $\times 5$ noise levels each). The density of $d = 0$ corresponds to noise-free images and of $d = 0.3$ is beyond the practically worst cases. Similarly, the Contrast data set contains 160 images, created by changing the background intensity of each of the 16 original synthetic images such that its contrast varies in 10 levels ranging from 1% to 20%. Here we adopt the definition of contrast introduced by Morrow et al. [46]

$$C_t = \frac{B_0 - B}{B_0 + B} 100\%, \tag{19}$$

where $B$ and $B_0$ are, respectively, the mean intensity of the object (foreground) and the surrounding region (background) in an image. In our real CT data, the contrast is about 8%. To our knowledge, CT images with the contrast of 20% are quite clear and those with the contrast of 1% are beyond the worst cases.

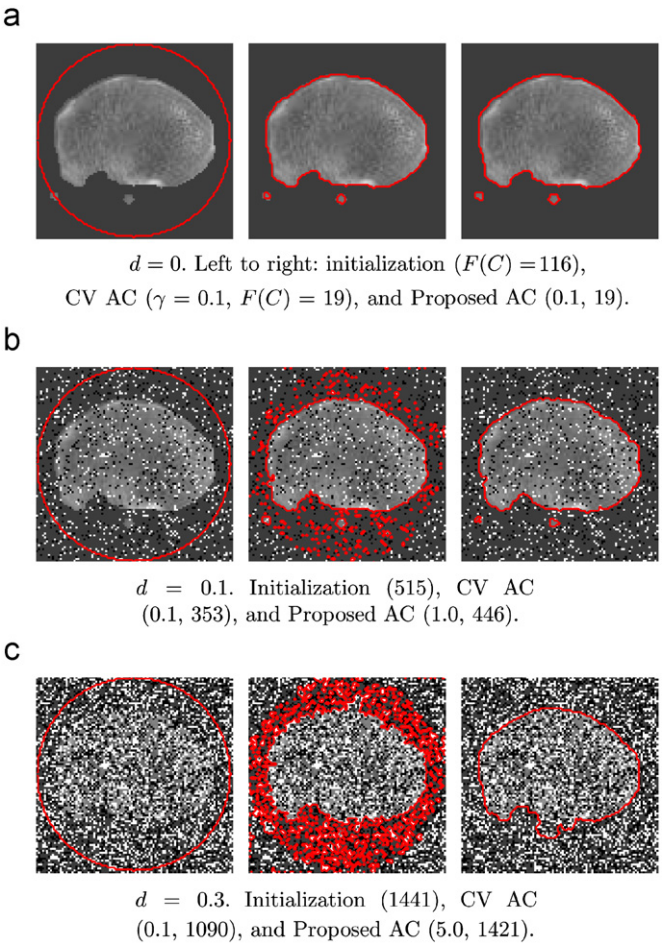


$d = 0$. Left to right: initialization ($F(C) = 116$), CV AC ($\gamma = 0.1$, $F(C) = 19$), and Proposed AC (0.1, 19).

$d = 0.1$. Initialization (515), CV AC (0.1, 353), and Proposed AC (1.0, 446).

$d = 0.3$. Initialization (1441), CV AC (0.1, 1090), and Proposed AC (5.0, 1421).

**Fig. 7.** Segmentation of a sample image with various noise densities. Average cpu time for each image is 84 s (CV AC) and 36 s (Proposed AC). This figure is in color in the electronic version.

### 3.2. Evaluation measure

We evaluate the quantitative performance using two error measures, $\varepsilon_1$ and $\varepsilon_2$, defined as

$$\varepsilon_1 = 1 - \frac{\#(\textit{Extracted regions} \cap \textit{True regions})}{\#(\textit{Extracted regions} \cup \textit{True regions})},$$

$$\varepsilon_2 = \mathrm{Hd}(\textit{Extracted boundaries}, \textit{True boundaries}), \tag{20}$$

where # denotes the number of points in a set and $\mathrm{Hd}(A, B)$ the Hausdorff distance between two polygons $A$ and $B$.

$$\mathrm{Hd}(A,B) = \max\{h(A,B), h(B,A)\}, \tag{21}$$

where $h(A,B) = \max_{a \in A} \min_{b \in B} \{dist(a,b)\}$ and $dist(a,b)$ is the Euclidean distance between points $a$ and $b$.

The error measure $\varepsilon_1$ quantifies the relative overlap between the segmented and the true regions and $\varepsilon_2$ measures the difference of the extracted and the true contours. The former provides a global goodness of the result, whereas the latter determines how much details of the object shape are captured. The more these measures are close to zero, the better the segmentation is.

## 4. Experimental results

In this section, we test the proposed model on various synthetic and real medical images in comparison with the conventional CV AC. The image feature, $I(\mathbf{x})$, employed is intensity. Both models share the same parameters $\eta$ and $\gamma$. Because $\eta$ is a constant used to shrink or expand the contour along its normal direction no matter where the contour is, increasing $\eta$ will make the contour likely pass weak edges though the evolution will be faster. Hence, for fair comparison, we choose $\eta = 0$ for both models. The other parameter $\gamma$, which

**Table 2**
$\gamma$ value settings for different noise densities.

| $d$ | 0 | 0.05 | 0.1 | 0.2 | 0.3 |
|---|---|---|---|---|---|
| Proposed AC | 0.1 | 1 | 1.5 | 3.5 | 5 |
| CV AC | 0.1 | [0.1, 1] | [0.1, 1.5] | [0.1, 3.5] | [0.1, 5] |

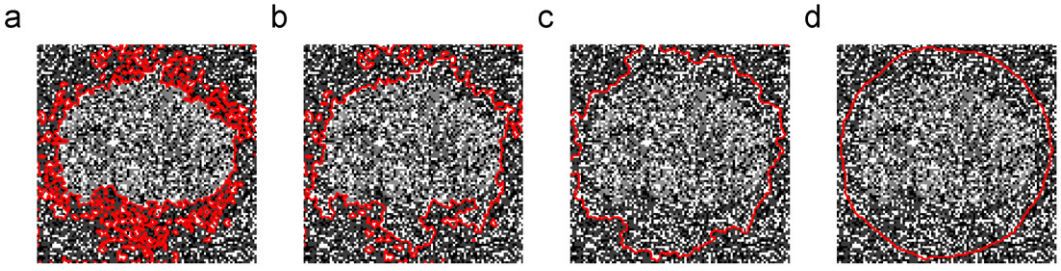


**Fig. 8.** CV AC's segmentation with different $\gamma$: (a) $\gamma = 0.2$, (b) 0.3, (c) 0.5, and (d) 5. The input image and the initialization are the same as Fig. 7(c).

weights the length constraint, is not the same for all experiments and will be specified in each case. If we want to detect as many objects as possible and of any size, $\gamma$ should be small. On the contrary, if we have to avoid extracting smaller objects (like points, due to noise), we should select a larger $\gamma$. The cpu time, in seconds, of our calculations performed on a Pentium IV Duo Core 1.87 GHz with 1GB of RAM will also be provided.

### 4.1. The phantom image

Let us get back to the phantom image in the example in Introduction. The curve is initialized in the same way as in Fig. 1(a) and the results with various $\beta$ values are shown in Fig. 3. It is possible to see that, with appropriate $\beta$, all four objects are detected, i.e., the "desirable" minimum of $F(C)$ is successfully found. The finding process with $\beta = 0.5$ is shown in Fig. 4 for a comparison against that in Fig. 2.

### 4.2. Sensitivity to $\beta$

Compared to the CV AC, our proposed AC introduces a new parameter, $\beta$. We can see from Fig. 3 that the proposed model can successfully detect the object with a large range of $\beta$. To investigate more thoroughly its sensitivity with respect to the $\beta$ parameter, we apply it on the real CT data set. Sample results are displayed in Fig. 5 and the quantitative evaluation is shown in Fig. 6. Again, it can be seen that this AC model is not much $\beta$-sensitive since it provides small error measures with many $\beta$ values ranging from 0.4 to 0.7. Consequently, we choose $\beta = 0.5$ for all follow-up experiments.

### 4.3. Sensitivity to noise

Fig. 7 shows that the CV AC works well with the noise-free image, but becomes stuck in the noise when available. Note the energy term $F(C)$; better results correspond to higher (more local minima) energy value. One may want to increase $\gamma$ to avoid the speckle noise. This works for the proposed AC, but not the CV AC. A higher $\gamma$ makes the CV AC unable to capture the fine-scale structure of the object as can be seen in Fig. 8(c)–(d). With that observation, we choose the appropriate $\gamma$ values proportional to the noise density as shown in Table 2. Here, the CV AC is tested with many values of $\gamma$ in the range (e.g., with $d$=0.05, we test the CV AC three times with $\gamma = \{0.1, 0.5, 1\}$) and the best results (in term of error measures) are reported in comparison with the proposed AC. The errors measures of the two models applied on the Salt-pepper data set are plotted in Fig. 9. We can see that the CV AC is more sensitive to noise than the proposed AC.

### 4.4. Sensitivity to contrast level

The Contrast data set is used to test the effectiveness of the proposed AC in segmenting low contrast objects. Fig. 10 shows segmentation of sample images having contrast of 20%, 11%, and 1%, respectively. Note that the region inside the little circle also belongs to the bone region, which is desirable target. At the contrast level of 20%, the two models have similarly good results.

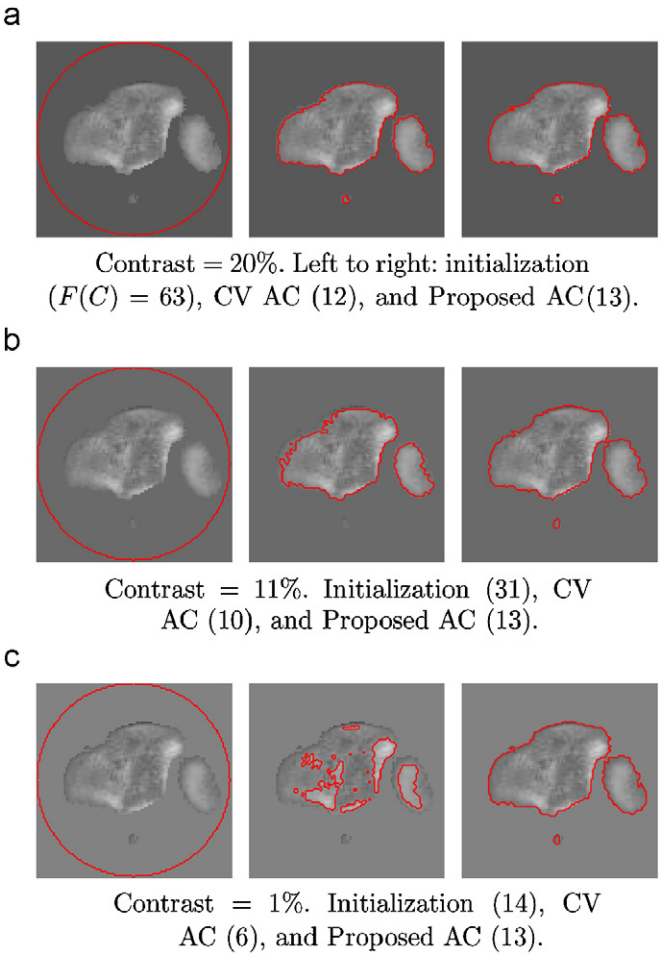


**Fig. 10.** Segmentation of a sample image with various contrast levels. $\gamma = 0.3$. Average cpu time for each image is 45 s (CV AC) and 25 s (Proposed AC). This figure is in color in the electronic version.

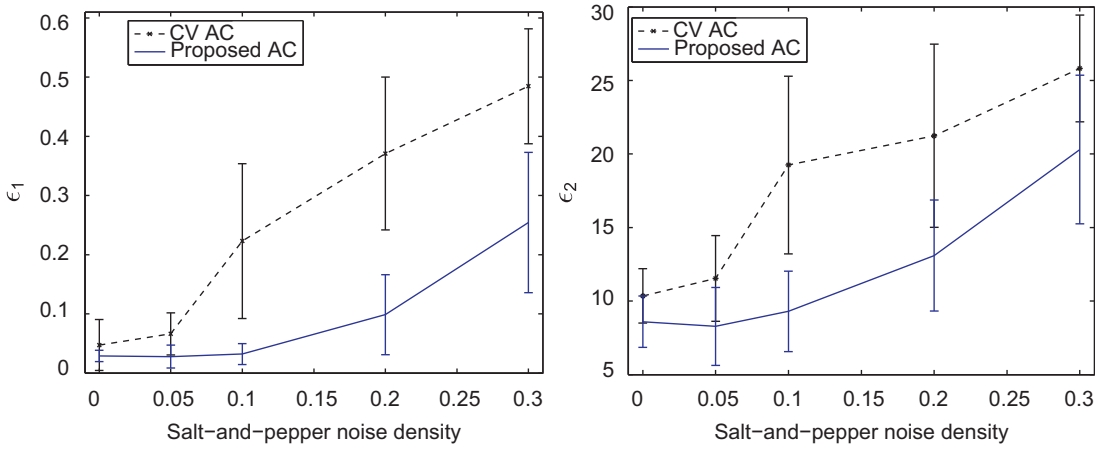


**Fig. 9.** Plots of error measures vs. noise density for the Salt-pepper data set. The proposed AC is less noise sensitive than the CV AC.

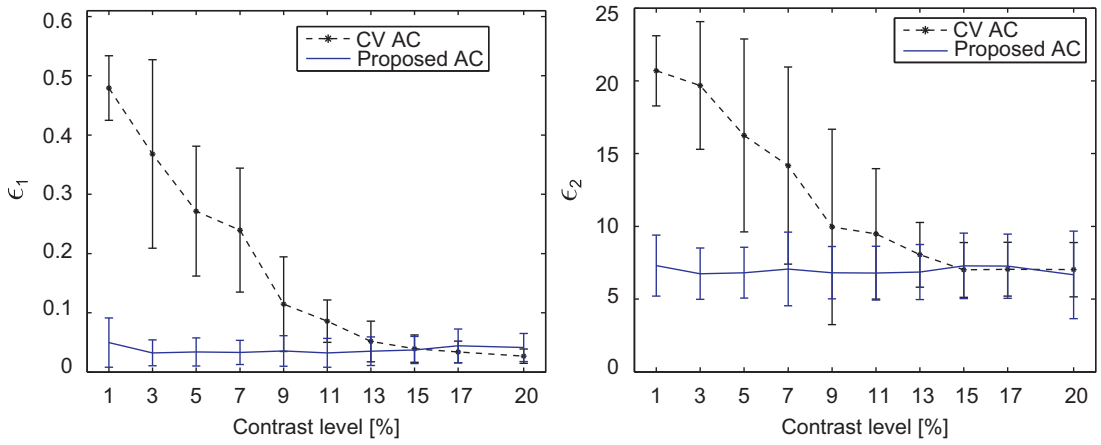


**Fig. 11.** Plots of error measures vs. contrast level for the Contrast data set. The proposed AC performs better than the CV AC, especially at low contrast levels.

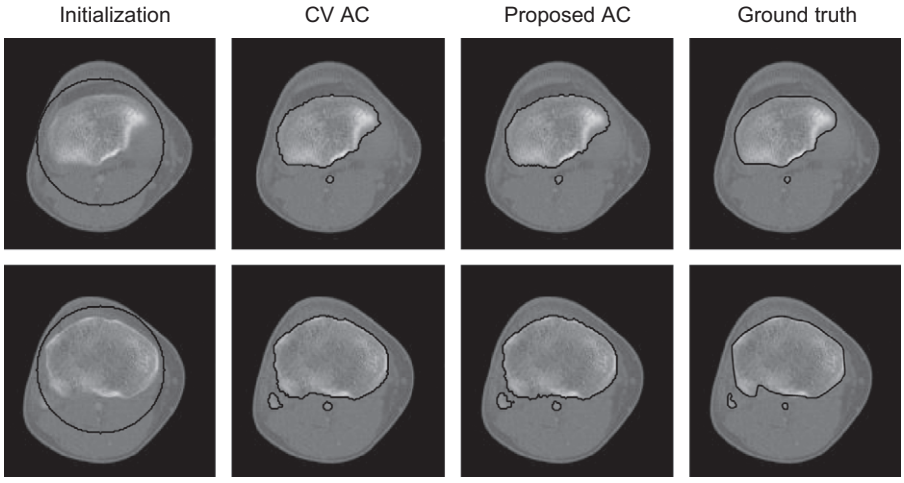


**Fig. 12.** Sample segmentation results for CT images. Average cpu time for each image is 47 s (CV AC) and 44 s (Proposed AC).

However, the CV AC's performance starts to decrease when the contrast level decreases, whereas the proposed AC's does not (see also Fig. 11).

### 4.5. *Performance with real medical images*

Figs. 12 and 13 show some sample segmentation results of the two models on CT and MRI images, respectively, and Table 3 displays the quantitative performance evaluated on these two whole data sets. It is observed that the proposed AC yields similar results to the CV model for the CT data set but performs significantly better when dealing with the MRI data set. One possible reason is that the testing MRI images are of lower contrast (see, e.g., the last row of Fig. 13). This is consistent with the experimental results obtained in Section 4.4.

## 5. Summary and discussion

A geometric AC model is usually built upon an image-dependent energy functional whose global minimum hopefully corresponds to a desirable solution as opposed to an undesirable result caused by noise or complex image structure. Unfortunately, as Li and Yezzi pointed out in their work [32], the desirable minimizers are often neither the most local nor the most global. In this paper, we have proposed a novel AC model based on a convex combination of the CV energy functional and the Bhattacharyya distance between the density functions inside and outside the curve. The resulting flow searches for a segmentation where both the difference within one segment is minimized and the distance between distinct segments are maximized. It is therefore more likely for the proposed model to reach desirable solution. The evolution flow of the proposed model is derived using the level-set framework, making it inherit advantages of a geometric AC such as topology adaptability.

Of course, incorporating another term means that we have introduced a new parameter which needs to be determined upon implementation. Fortunately, experimental results showed that the proposed model is not very sensitive to this new parameter, i.e., it could generate desirable results with a large range of the parameter's value (see, e.g., Section 4.2).

One of the advantages of the CV AC over other geometric AC models is that it can be initialized outside, inside, or even across the objects of interest because its force $V_N$ can flexibly and automatically change its direction during evolution (from negative to positive and vice versa, depending on the current curve's position) as opposed to the fixed direction of $V_N$ in other models. Our model also inherits this great advantage. Thus, in the experiments, although the two models would work with other initialization schemes, the "outside" initialization was selected for its more intuitive form and again, for fair comparison.

Compared with the conventional CV model, the proposed AC mostly performs better and is less sensitive to noise and contrast

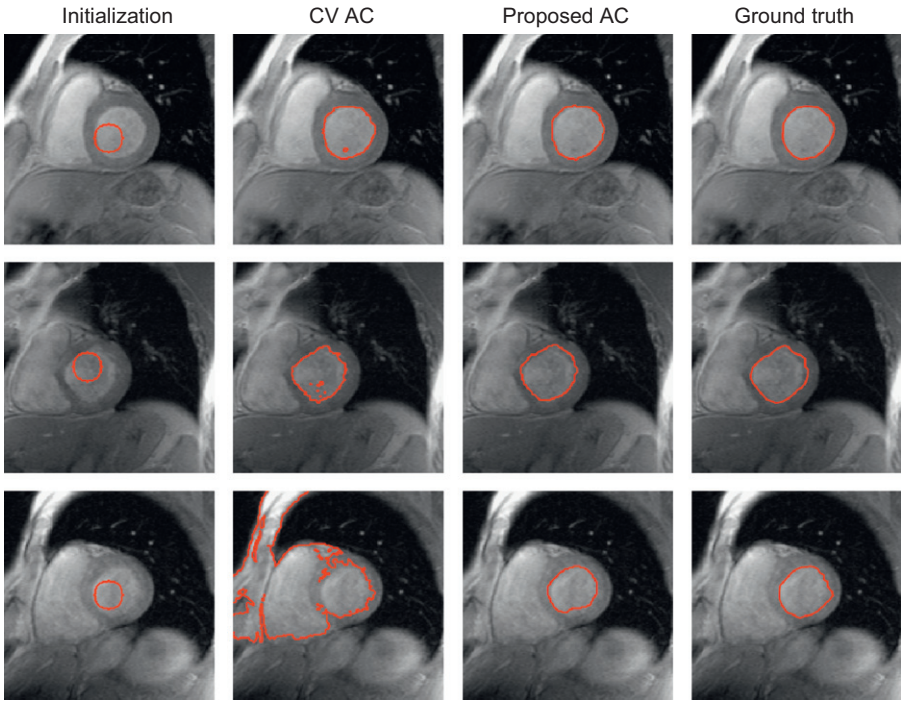


**Fig. 13.** Sample segmentation results for MRI images. Average cpu time for each image is 65 s (CV AC) and 52 s (Proposed AC). This figure is in color in the electronic version.

**Table 3**
Mean and SD of error measures for real medical data sets.

| | $\overline{\varepsilon_1}, \overline{\varepsilon_2}$ $(SD_1, SD_2)$ | |
|---|---|---|
| | CT data | MRI data |
| CV AC | 0.086, 6.764 (0.016, 1.542) | 0.309, 20.387 (0.159, 11.860) |
| Proposed AC | 0.089, 7.120 (0.013, 1.537) | 0.148, 6.097 (0.038, 2.342) |

Note: $SD_i = SD(\varepsilon_i)$, $i = \{1, 2\}$.

levels. It is also possible to see that the cpu time of our model is comparable to or even less than that of the CV AC despite the higher computational cost. This is due to the fact that the additional evolving term helps to move the curve faster towards convergence. As a conclusion, we consider it a good candidate for unsupervised medical image segmentation, where the images are usually noisy and low-contrast.

## Conflict of interest statement

None declared.

## Acknowledgement

This work was supported by a grant from the Kyung Hee University in 2009 (KHU-20090439).

## References

[1] T.M. Peters, Image-guidance for surgical procedures, Phys. Med. Biol. 51 (2006) 505–540.
[2] L. Wang, M. Greenspan, R. Ellis, Validation of bone segmentation and improved 3-D registration using contour coherence in CT data, IEEE Trans. Med. Imag. 25 (2006) 324–334.
[3] J. Zhang, C.-H. Yan, C.-K. Chui, S.-H. Ong, Fast segmentation of bone in CT images using 3D adaptive thresholding, , Comput. Biol. Med. 40 (2) (2010) 231–236.
[4] K. Levinski, A. Sourin, V. Zagorodnov, Interactive surface-guided segmentation of brain MRI data, Comput. Biol. Med. 39 (12) (2009) 1153–1160.
[5] M. Lynch, O. Ghita, P. Whelan, Automatic segmentation of the left ventricle cavity and myocardium in MRI data, Comput. Biol. Med. 36 (4) (2006) 389–407.
[6] G. Boccignone, P. Napoletano, V. Caggiano, M. Ferraro, A multiresolution diffused expectation-maximization algorithm for medical image segmentation, Comput. Biol. Med. 37 (1) (2007) 83–96.
[7] R. Gonzalez, R. Woods, Digital Image Processing, Prentice-Hall, New Jersey, USA, 2002.
[8] J. Canny, A computational approach to edge detection, IEEE Trans. Pattern Anal. Mach. Intell. 8 (1986) 679–698.
[9] J. Beveridge, J. Griffith, R. Kohler, A. Hanson, E. Riseman, Segmenting images using localized histograms and region merging, Int. J. Comp. Vis. 2 (1989) 311–352.
[10] D. Mumford, J. Shah, Optimal approximation by piecewise smooth functions and associated variational problems, Commun. Pure Appl. Math. 42 (1989) 577–685.
[11] M. Kass, A. Witkin, D. Terzopoulos, Snakes: active contour models, Int. J. Comp. Vis. 1 (4) (1988) 321–331.
[12] L. Cohen, I. Cohen, Finite element methods for active contour models and balloons for 2D and 3D images, IEEE Trans. Pattern Anal. Mach. Intell. 15 (11) (1993) 1131–1147.
[13] S. Zhu, A. Yuille, Region competition: unifying snakes, region growing, and Bayes/MDL for multiband image segmentation, IEEE Trans. Pattern Anal. Mach. Intell. 18 (1996) 884–900.
[14] C.S. Poon, M. Braun, Image segmentation by a deformable contour model incorporating region analysis, Phys. Med. Biol. 42 (1997) 1833–1841.
[15] C. Xu, J. Prince, Snakes, shapes, and gradient vector flow, IEEE Trans. Image Proc. 7 (1998) 359–369.
[16] F. Leitner, P. Cinquin, Dynamic segmentation: detecting complex topology 3D objects, in: Proceedings of Engineering in Medicine and Biology Society, 1991.
[17] R. Szeliski, D. Tonnesen, D. Terzopoulos, Modeling surfaces of arbitrary topology with dynamic particles, in: Proceedings of CVPR, 1999, pp. 82–87.
[18] T. McInerney, D. Terzopoulos, T-snakes: topology adaptive snakes, Med. Image Anal. 4 (2) (2000) 73–91.
[19] V. Caselles, F. Catte, T. Coll, F. Dibos, A geometric model for active contours in image processing, Numer. Math. 66 (1993) 1–31.
[20] V. Caselles, R. Kimmel, G. Sapiro, Geodesic active contours, Int. J. Comp. Vis. 22 (1997) 61–79.

[21] K. Siddiqi, Y.B. Lauziere, A. Tannenbaum, S.W. Zucker, Area and length minimizing flows for shape segmentation, IEEE Trans. Image Proc. 7 (3) (1998) 433–443.
[22] T. Chan, L. Vese, Active contours without edges, IEEE Trans. Image Proc. 10 (2001) 266–277.
[23] L. Vese, T. Chan, A multiphase level set framework for image segmentation using Mumford and Shah model, Int. J. Comp. Vis. 50 (3) (2002) 271–293.
[24] N. Paragios, O. M-Gottardo, V. Ramesh, Gradient vector flow fast geometric active contours, IEEE Trans. Pattern Anal. Mach. Intell. 26 (2004) 402–407.
[25] J. Sethian, Level Set Methods and Evolving Interface in Geometry, Computer Vision, Cambridge University Press, New York, USA, 1996.
[26] S. Osher, R.P. Fedkiw, Level Set Methods and Dynamic Implicit Surfaces, Springer-Verlag, New York, USA, 2003.
[27] R. Malladi, J.A. Sethian, B.C. Vemuri, Shape modeling with front propagation: a level set approach, IEEE Trans. Pattern Anal. Mach. Intell. 17 (2) (1995) 158–175.
[28] M. Rousson, N. Paragios, Shape priors for level set representations, in: ECCV, Springer, 2002, pp. 78–92.
[29] D. Cremers, F. Tischhauser, J. Weikert, C. Schnorr, Diffusion snakes: introducing statistical shape knowledge into the Mumford-Shah functional, Int. J. Comp. Vis. 50 (3) (2002) 295–313.
[30] A. Tsai, A. Yezzi, A. Wells, C. Tempany, D. Tucker, A. Fan, W. Grimson, A. Willsky, A shape-based approach to the segmentation of medical imagery using level sets, IEEE Trans. Med. Imag. 22 (2) (2003) 137–154.
[31] N. Paragios, R. Deriche, Geodesic active regions and level set methods for supervised texture segmentation, Int. J. Comp. Vis. 46 (3) (2002) 223–247.
[32] H. Li, A. Yezzi, Local or global minima: flexible dual-front active contours, IEEE Trans. Pattern Anal. Mach. Intell. 29 (2007) 1–14.
[33] A. Tsai, A. Yezzi, A. Willsky, Curve evolution implementation of the Mumford-Shah functional for image segmentation, denoising, interpolation, and magnification, IEEE Trans. Image Proc. 10 (8) (2001) 1169–1186.
[34] J. Piovano, M. Rousson, T. Papadopoulo, Efficient segmentation of piecewise smooth images, in: F. Sgallari, A. Murli, N. Paragios (Eds.), Scale Space and Variational Methods in Computer Vision, Lecture Notes in Computer Science, vol. 4485, Springer, Berlin/Heidelberg, 2010, pp. 709–720.
[35] P.T.H. Truc, S.-Y. Lee, T.-S. Kim, A density distance augmented Chan–Vese active contour for CT bone segmentation, in: 30th Annual International Conference of IEEE in Medicine and Biology Society, 2008, pp. 482–485.
[36] N. Houhou, J.-P. Thiran, X. Bresson, Fast texture segmentation based on semi-local region descriptor and active contour, Numerical Mathematics: Theory, Methods and Applications 2 (4) (2009) 445–468.
[37] K. Ni, X. Bresson, T. Chan, S. Esedoglu, Local histogram based segmentation using the Wasserstein distance, Int. J. Comput. Vision 84 (1) (2009) 97–111.
[38] T. Kailath, The divergence and Bhattacharyya distance measures in signal selection, IEEE Trans. Commun. Technol. 15 (1967) 52–60.
[39] K. Fukunaga, Introduction to Statistical Pattern Recognition, second ed., Academic Press Professional, Inc., 1990.
[40] F. Goudail, P. Refregier, G. Delyon, Bhattacharyya distance as a contrast parameter for statistical processing of noisy optical images, J. Opt. Soc. Am. A 21 (7) (2004) 1231–1240.
[41] D. Freedman, T. Zhang, Active contours for tracking distributions, IEEE Trans. Image Proc. 13 (7) (2004) 518–526.
[42] D. Comaniciu, V. Ramesh, P. Meer, Kernel-based object tracking, IEEE Trans. Pattern Anal. Mach. Intell. 25 (5) (2003) 564–577.
[43] O. Michailovich, Y. Rathi, A. Tannenbaum, Image segmentation using active contours driven by the Bhattacharyya gradient flow, IEEE Trans. Image Proc. 16 (11) (2007) 2787–2801.
[44] H.-K. Zhao, T. Chan, B. Merriman, S. Osher, A variational level set approach to multiphase motion, J. Comput. Phys. 127 (1996) 179–195.
[45] M.B. Stegmann, An annotated dataset of 14 cardiac MR images, Technical Report, Technical University of Denmark, 2002.
[46] W.M. Morrow, R.B. Paranjape, R.M. Rangayyan, J.E.L. Desautels, Region-based contrast enhancement of mammograms, IEEE Trans. Med. Imag. 11 (1992) 392–406.